Surface flow and vortex shedding of an impulsively started wing

By R. F. HUANG[1], J. Y. WU[1], J. H. JENG[1] AND R. C. CHEN[2]

[1]Department of Mechanical Engineering, National Taiwan University of Science
and Technology, Taipei, Taiwan 10672, Republic of China
e-mail: rfhuang@mail.ntust.edu.tw

[2]Department of Mechanical and Marine Engineering, National Taiwan Ocean University,
Keelung, Taiwan, Republic of China

The particle tracking flow visualization method (PTFV) and particle image velocimetry (PIV) are used to obtain a clear picture of vortex evolution on the suction surface of an impulsively started NACA 0012 wing. The experiments are conducted in a towing water tank. The formation, evolution, and shedding of the vortex system on the suction surface are observed and analysed by streak pictures of particle images. Five characteristic vortex evolution regimes are identified in the parameter domain of angle of attack and chord Reynolds number. The pathline patterns, instantaneous streamlines, and vorticity of various vortex evolution processes are presented. Stable vortex shedding in the wake is eventually established after the initial period of complex vortex evolution on the suction surface of the wing. Various types of instabilities in the wake, e.g. instability wave, surface vortex shedding, and bluff-body vortex shedding, are found to correspond to different evolution processes of the surface flow. The shedding frequency of the vortices is correlated and compared with several conventional results. Topological critical points, separatrices, and alleyways are identified and discussed to elucidate the unsteady structure of the instantaneous streamline patterns. The topological rule for the number of singular points is verified.

1. Introduction

The wing model serves as an excellent tool for the investigation of surface flow and wakes because it varies from a slender body to a bluff body as the angle of attack varies from low to high. When an airfoil is started from rest, unsteady effects will cause large spatial and temporal gradients in the flow so that considerably different phenomena from those observed in a flow passing over a static airfoil (Lissaman 1983; Arena & Mueller 1980) are usually anticipated.

Many investigations employing qualitative or quantitative flow visualization techniques and computational methods have been conducted on the early stage of a circular cylinder started from rest, e.g. Williamson (1996), Coutanceau & Menard (1985), Ta Phuoc Loc & Bouard (1985), Chu & Liao (1992), and Chu *et al.* (1996). Chu & Liao used a laser-induced photochemical anemometer to probe the time-varying velocity distributions behind a circular cylinder started from rest. They found that the far-field velocity and vorticity distributions provide information on the process of vortex shedding in the cylinder wake. The vortex shedding process has been topologically analysed with critical point theory in two-dimensional flows (Perry,

Chong & Lim 1982; Perry & Steiner 1987; Steiner & Perry 1987). Saddles and foci were found to feature and helped to elucidate the dynamic flow fields. Sumner, Proce & Paidoussis (1997) used a particle image velocimeter to measure the time history of the instantaneous in-plane vorticity field around impulsively started side-by-side circular cylinders. The strength and paths of vortices were also obtained. However, the eventual status and link between the evolution of the dynamic vortical structures and vortex shedding in the wake were not addressed.

Nair & Sengupta (1997) solved numerically the unsteady flow past a fixed elliptic cylinder. For quite complex flows, different types of bubble formation (single and multiple bubbles) and their movements over the body are obtained. Also, a trailing-edge vortex induced by the release of vortices in the neighbourhood of the trailing edge is observed. The trailing-edge vortex is essentially an unsteady phenomenon, i.e. streamlines on the pressure surface wrap around the vortices over the suction surface, caused by the flow acceleration and detachment from the suction surface. They concluded that the release frequency of vortices in the wake is a function of the angle of attack and type of bubble formation. Ohmi *et al.* (1990, 1991) studied the starting flow past an oscillating and translating elliptical cross-sectional cylinder at deep stall by means of visualization experiments and numerical calculations. The evolution of vortical structures on the suction surface of an oscillating wing was described qualitatively. After the detachment of a starting vortex, an initial separation bubble develops into a large-scale vortex spreading over the whole suction surface. This vortex detaches slowly from the elliptic cylinder, drawing the pressure-surface separating flow up from behind the trailing edge. They found that the starting flow at low reduced oscillating frequencies in general preserves the fundamental characteristics of the static stall, which is usually observed for a high-incidence fixed elliptic cylinder. The vortical wakes are generated primarily by the action of the translating flow.

Most of the investigations on the impulsively started wing employ qualitative flow-visualization methods and/or various computational schemes (Ohmi *et al.* 1990). Ohmi *et al.* (1991) have studied vortex formation around a NACA 0012 airfoil oscillating and translating at large incidences. At low reduced oscillating frequencies, no substantial differences between the wakes of the NACA 0012 airfoil and elliptic cylinder are found: the initial wake is initially unsteady, consisting of the development of a large-scale leading-edge vortex over the suction surface, followed by detachment of the vortex, establishment of suction-surface reverse streamlines in the shape of an inverted S, and subsequent development and shedding of the smaller trailing-edge vortex. Coutanceau & Pineau (1997) is an excellent review of the time-evolution of vortical structures behind various bluff bodies.

There have been many studies over the years on the nature of unsteady flow in the wake of an airfoil. The wake behind an airfoil usually consists of instability waves and coherent structures with periodic unsteady motions, depending on the Reynolds number and the angle of attack. The unsteady wake of an airfoil at large angles of attack and Reynolds numbers was found to behave similarly to that of a bluff body (Brooks & Schlinker 1983). The Kármán-type vortex street behind an airfoil has been discussed by Stuber & Gharib (1988). For airfoils at low angles of attack and Reynolds numbers, a wake with the characteristics of a mixing layer developing spatially from instability waves of small amplitude to rolled-up vortices was observed (Huang & Lin 1995). As the viscous forces are not negligible when analysing the evolution of the instability waves at the initial stage of the spatially developing vortex street in a free shear layer (Oertel 1990), the frequency characteristic of the mixing layer is different from that of a bluff-body wake.
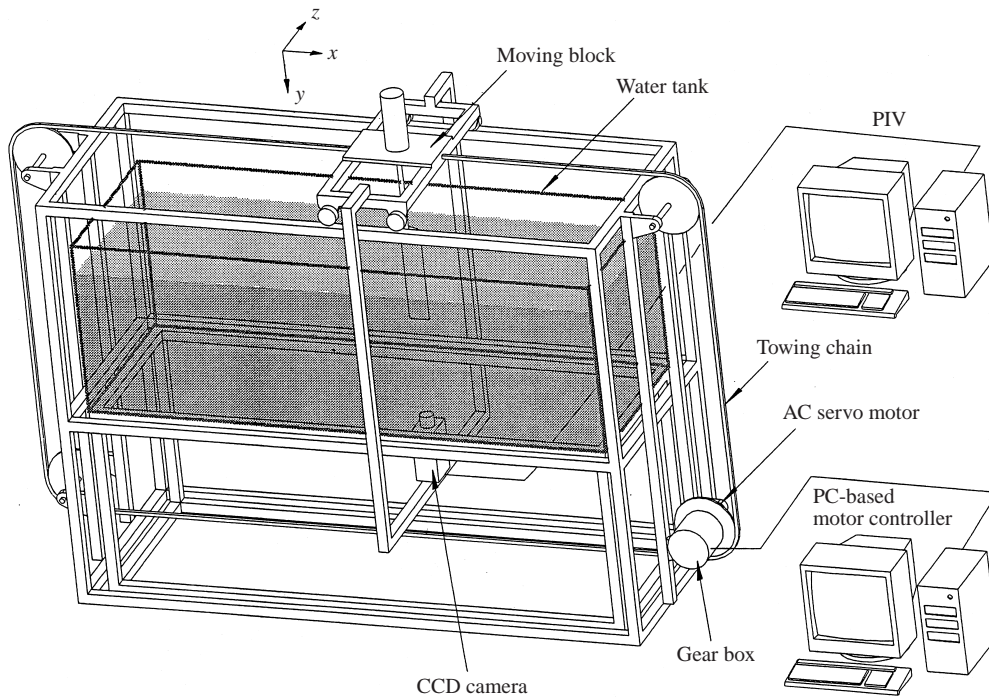
FIGURE 1. Experimental setup.

The evolution of the large structures on the suction surface of a wing started from rest is important for the unsteady aerodynamic loads at the early stage of operation. Also, the evolution of surface vortices may imply the formation of unsteady structure in the wake. However, the literature discussing the detailed behaviour, dominant mechanism, and frequency characteristics of the unsteady wake behind an airfoil is limited. In this paper, experimental results on the surface flow, a topological critical point analysis, and the frequency characteristics of vortex shedding of a NACA 0012 wing are presented. The frequency of vortex shedding is correlated to assist the interpretation of the experimental results and the dominant mechanism. The objectives are to elucidate: (i) vortex evolution on the suction surface of an impulsively started wing; (ii) the establishment of the vortex wake; (iii) the correlation of the shedding frequency of vortices in the wake.

2. Experimental arrangements

2.1. *Apparatus*

The experiments were conducted in a transparent, open-top, rectangular water tank ($60 \times 60 \times 210\,\mathrm{cm}^3$) with a closed-loop towing mechanism surrounding it, as shown in figure 1. The inner endwalls of the water tank, not shown in the figure, were lined with thick layers of sponge and three layers of appropriately spaced screens to reduce the reflection of incident waves from the endwalls. The water in the tank was allowed to settle before the execution of an experimental run.

A moving block, which serves to carry objects, is sited on two carefully calibrated parallel stainless rails. The stainless rails are in turn mounted on a steel chassis over the top of the water tank. The moving block is dragged by a metal sprocket-chain,
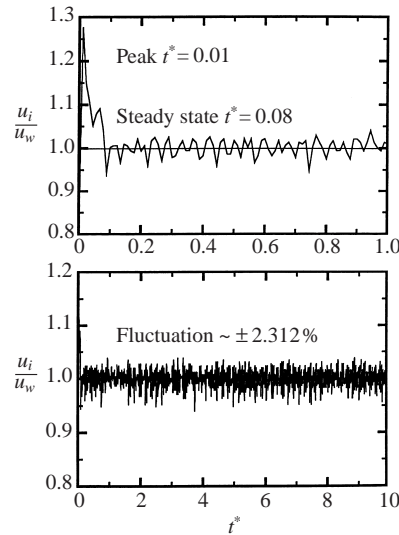
FIGURE 2. Velocity characteristics of towing motion.

which is driven by an AC servomotor. The motion of the servomotor is controlled by a PC-based feedback controller. Artificial intelligent and neuro-fuzzy techniques are incorporated into the computer program so that the controller can automatically correct its control parameters to obtain optimized parameters after the first trial run. Typical normalized instantaneous towing velocity u_i/u_w is shown in figure 2. The symbols u_i and u_w denote the instantaneous and average towing velocities of the wing model, respectively. The normalized instantaneous velocity after the start of motion attains a peak value of 1.28 at the reduced time $t^* = 0.01$. The reduced time t^* is defined as tu_w/C, where t is the time from start and C is the chord length of wing model. Steady state is reached at $t^* = 0.08$. The standard deviation of the normalized velocity fluctuation after the steady state of velocity is reached is about $\pm 2.3\%$. In the operation range of this study, the towing performance at all speeds has similar properties.

A NACA 0012 straight wing model (Abbot & Von Doenhoff 1959) made of aluminium alloy is mounted under the moving block. The wing model has a chord length $C = 6$ cm and a span $S = 30$ cm so that the aspect ratio is 5. Its surface is anodized black to avoid scattering of laser light. The coordinate system adopted is shown in the upper-left corner of figure 1. Symbols x, y and z denote the streamwise, spanwise, and cross-stream coordinates, respectively, with origin at the leading edge of the wing on the root-plane. The impulsively started linear towing motion is in the $+x$-direction and the span is in the $+y$-direction pointing downward.

A rigid steel frame surrounds the water tank, as shown in figure 1. A CCD camera facing the $-y$-direction is mounted on the bottom of the steel frame so that the camera can move steadily with the motion of the moving block and the image frame always aims at the same view window. The laser beam from an argon-ion laser is transmitted through an optical fibre and then connected to a $20°$ laser-light-sheet expander, mounted on the side rod of the outer steel frame, so that the camera, wing model and laser-light sheet all move in-phase. The laser-light sheet is adjusted to a thickness of about 0.5 mm.

Plastic particles made of polyamide (PM) are seeded in the water tank to scatter

the laser light. The diameters of particles are between 30 and 70 μm and the specific weight is 1.03 at 25 °C. Ignoring the effect of turbulent diffusion, the relaxation time constant is estimated to be less than 6.25×10^{-5} s and Stokes number is of order 10^{-6} within the range of experiment so that slip between the flow and particles could be neglected (Richard & John 1988; William 1982).

The particle images are recorded by a Sony SSC-M370 frame-transfer CCD camera with a resolution of 768×494 pixels, which is equipped with an asynchronous variable electronic shutter, with speed ranging from 1/60 to 1/10 000 s. During the experiment the shutter speed and the framing rate are set at 1/2000 s and 30 frames per second, respectively. A Data Translation DT-2861 frame grabber board digitizes the analogue voltage output from the CCD array of the camera. The maximum frame-grabbing rate is 30 frames s^{-1}. Each frame consists of two interlaced video fields (even and odd) with a time interval of 1/60 s. A detailed description of the locating and matching of particle images and the computing of velocity vectors can be found in Chen & Fan (1992); only a short description is provided here. The digitized frames are first processed to eliminate background and electronic noises by using a grey level threshold in order to improve image quality. A scanning subroutine then begins to identify the particle image by locating a pixel with a non-zero grey value and conducts an image boundary search to locate all corners of the particle image. Once the boundary of the particle image is identified, the centroid and equivalent mean diameter of the particle image are computed. A procedure to find the instantaneous displacement vectors is then executed. It requires an estimation of maximum particle displacement and direction tolerances. The subroutine scans for the identified centroids on a sub-field. Once a centroid is located, the subroutine searches the next adjacent sub-field for possible centroids located around the identified centroid. The range of search is based on the prescribed maximum magnitude and direction tolerances of particle displacement vectors. Once it computes and records the displacement between two qualified centroids on adjacent sub-fields, a search for particles on the third adjacent sub-field starts. If a particle with the allowed displacement and direction tolerance is found in the third sub-field, the subroutine identifies the three successive sub-fields as being a matched sequence. If this is not the case, the search is discarded and the procedure goes back to the first sub-field to search for another identified centroid. The subroutine continues until all particle images of the first sub-field are scanned. With the assumption of linear and constant flows during the short recording intervals, the velocities of particle images are obtained by dividing recorded displacements by time interval between adjacent sub-fields.

2.2. *Error analysis*

The 'instantaneous' velocities are calculated based on the movement of particles for three consecutive field intervals, namely, 2/60 s. The calculated velocity vectors are then assumed to be the instantaneous ones for the first frame. In the current field of view ($\approx 10 \times 7.5$ cm^2), each seeding particle will occupy less than one pixel and the uncertainty in locating the centroids can be reasonably estimated as $\pm 1/2$ pixel. Since most of the detected particle displacements are over 6 pixels, the estimated errors of velocity vectors are at most around 8%.

The interpolation process uses the inverse-distance weighting algorithm

$$\hat{V}_p = \sum_{i=1}^{n} W_i \hat{V}_i \bigg/ \sum_{i}^{N} W_i, \tag{1}$$

for each velocity vector frame. $\hat{V}_i$ is the measured velocity, $\hat{V}_p$ is the interpolated velocity at node point p, and W_i is the weighting function. The weighting function employed in the present study is $1/r^2$, where r is the distance between the location with measured velocity $\hat{V}_i$ and the node to be interpolated. According to Davis (1986), the estimation variance s_e^2 of an interpolated velocity at location p can be approximated as

$$s_e^2 = (\hat{V}_p - V_p)^2 \approx \sum_{i=1}^{n} W_i \gamma(h_{ip}) \Big/ \sum_{i=1}^{N} W_i, \qquad (2)$$

where the standard estimation error $s_e = \sqrt{s_e^2}$; $\hat{V}_p$ is the interpolated velocity and V_p is the 'true' one. In (2) $\gamma(h_{ip})$ is the semi-variance over a distance h_{ip} between control points p and i. It can be estimated as

$$\gamma(h_{ip}) = \frac{\sum(\hat{V}_p - \hat{V}_{p+h})^2}{2n}, \qquad (3)$$

which is the sum of the squared differences between measured velocities $(\hat{V}_p, \hat{V}_{p+h})$ of pairs of points (n pairs in total) separated by a distane h_{ip}. Using this approximation, the ratios between the standard errors and the interpolated velocities (i.e. $s_e/\hat{V}_p$) are approximately between 15% and 20% in the very low-velocity region because of the denominator. In the large-velocity region, the error is much lower than 15%. This estimation of error is in general consistent with the analysis conducted by Spedding & Rignot (1993) using the weighting function $W_i = 1/r$. Note that, as also concluded in Spedding & Rignot, the difference between two interpolated flow fields in the velocity and vorticity fields are small, with 11.1% and 6.4% errors, respectively. Therefore, it can be assumed that the current work is able to reveal macro flow information despite the local micro flow structure perhaps being more or less smeared out. According to error propagation theory and also as confirmed by Spedding & Rignot, the vorticities have the same uncertainty level as the interpolated velocities under the assumption that the uncertainties in measuring the grid distances Δx and Δy are relatively small and can be neglected.

3. Results and discussion

3.1. *Determination of imaging plane*

Before the experiments are conducted, the effects of free surface of the water and the free end of the wing on the two-dimensionality of the surface flow and vortex shedding are carefully examined. The water is filled up to the level $y/C = 0.5$. The free surface of the water is maintained clean so that the contamination-induced end bowing (Slaouti & Gerrard 1981) of the two-dimensional vortex shedding in the wake is almost negligible. The results show that neither the surface flow nor vortex shedding are affected, at least from $y/C \approx 0.6$ to 3.3. Above this, it is observed that the downwash effect near the wing tip alters the vortical motion on the surface and suppresses the vortex shedding in the wake. For instance, at $y/C = 3.7$ the vortical motion on the wing surface slows down so that the shedding frequency of vortices is decreased by about 25%. At $y/C > 4.4$, the vortical motion on the wing surface and periodical vortex shedding in the wake are completely suppressed. The area influenced by end effects spanned at most from $y/C \approx 3.3$ to 5. The imaging plane is chosen to be $y/C = 2.1$, which is in the range of $y/C = 0.6$–3.3, where the free-surface and end effects are not significant. Because from a topological point of view (Perry & Steiner
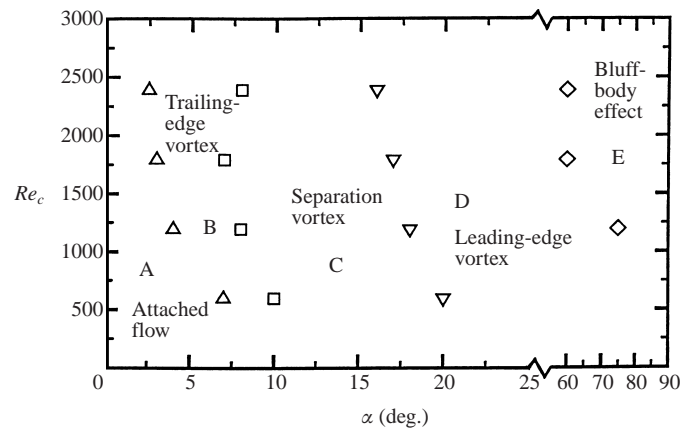
FIGURE 3. Characteristic modes of surface flow evolution identified on the parameter domain of chord Reynolds number/angle of attack.

1987) a precisely two-dimensional and precisely symmetrical flow patterns are unlikely ever to occur in practice, the imaging plane is in reality nominally two-dimensional.

3.2. *Evolution of surface vortices*

The particle tracking flow visualization method is employed first to search for possible characteristic modes of the vortex evolution process on the wing surface. The pathlines of the particle images are recorded on streak films with long exposure time and low framing rate. The images are also recorded on video tapes with short exposure time ($1/2000$ s) and high framing rate (30 f.p.s.). Identification and analysis of the formation and evolution of the vortex system on the suction surface are then conducted either by replaying the movies of particle images on a TV monitor or by tracing the long-exposure streak pictures.

It is well known that, for an unsteady flow, the particle trajectories in general do not coincide with streamlines except over short time intervals (Chong & Perry 1990). Therefore the short-exposure video movies may properly represent the continuous motions of streamlines (Perry *et al.* 1982). However, the long-exposure particle trajectories, which contain many pathline segments, may not appropriately represent instantaneous streamlines. For a wing with a chord length of 6 cm, towed at a velocity of $2\,\mathrm{cm\,s^{-1}}$, the characteristic time scale of the large eddies is estimated to be about 3 s. If the exposure time is 0.5 s, which is about 16% of the characteristic time scale of large eddies, then the streak pathline patterns may not be able to show the instantaneous streamlines exactly. Experimentally, the frequency of vortex shedding at velocity $2\,\mathrm{cm\,s^{-1}}$ varies from 0.05 to 0.1 Hz at different angles of attack so that the characteristic time scales of the large eddies vary from about 10 to 20 s. The exposure time of 0.5 s thus is about 2.5% to 5% of the time scale of large flow structures. The deviation of the pathlines from streamline patterns hence should not be significant and should be clear enough to elucidate the evolution of large eddies.

Five different regimes in the evolution of surface flow are identified in the parameter domain of chord Reynolds number Re_c and angle of attack α, as shown in figure 3. They are: *attached flow* (type A), *trailing-edge vortex* (type B), *separation vortex* (type C), *leading-edge vortex* (type D), and *bluff-body effect* (type E).

The *attached flow* is observed at very low angles of attack and towing velocity. The surface flow is always attached to the suction surface no matter how long the
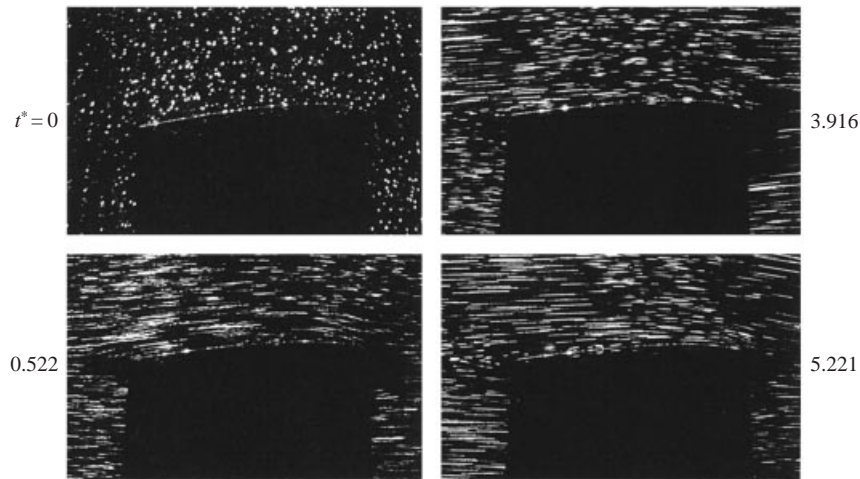
FIGURE 4. Streak pictures at $Re_c = 1200$, $\alpha = 2°$, attached flow, exposure time: 0.5 s.

time evolves, as shown in the streak pictures of figure 4. No separation or vortical structures are found on the wing surface.

The *trailing-edge vortex* mode occurs where the angle of attack is larger than that of the attached flow and smaller than the stall angle, 10°, of the NACA 0012 wing at small Reynolds numbers reported by Huang *et al.* (1996). Figure 5 shows typical streaklines of the flow on the suction surface. At the initial stage after the start of the wing model, the surface flows remain attached. Then the originally attached flows on the suction surface separate from the trailing edge, as shown in the picture at $t^* = 2.087$. As time evolves, the separation point moves gradually upstream. A counter-clockwise-rotating vortex wrapping from the pressure surface to the suction surface near the trailing edge (called the 'trailing-edge vortex') and a clockwise-rotating vortex (called the 'surface vortex') in the separated shear layer are formed, as shown in the pictures at $t^* = 3.392$ and 3.915. The counter-clockwise-rotating trailing-edge vortex leaves the wing surface, while the clockwise-rotating surface vortex grows as it rolls towards the trailing edge, as shown at $t^* = 4.437$ and 4.959. A trailing-edge vortex is seen at $t^* = 5.481$ as the surface vortex is leaving the wing surface. The trailing-edge vortex then grows as time evolves, as shown at $t^* = 5.742$ and 6.003. Alternating downstream shedding of a trailing-edge vortex and a surface vortex from the wing surface becomes periodical. The sequence of flow-structure motion before the periodical vortex shedding is established includes a starting vortex, boundary-layer separation, a trailing-edge vortex and a surface vortex.

The *separation vortex* is observed in regime C of figure 3, where the angles of attack are greater than the stall angle (Huang *et al.* 1996). Figure 6 shows typical streaklines of surface flows on the suction surface. When $t^* > 1$, the boundary-layer separates from the trailing edge similarly to type B. The separation point moves upstream as time evolves. Surface vortices are formed in the separated boundary layer due to the increase of vorticity induced by the reverse flow, as shown in the picture at $t^* = 1.564$. The surface vortex rolls downstream, entrains circumferential fluid, and enlarges as time evolves, as shown at $t^* = 1.825$, and 3.131. As the vortex reaches the trailing edge and is about to escape, the large sub-atmospheric pressure and shear effect induce a trailing-edge vortex to wrap from the pressure surface to the suction surface, as shown at $t^* = 3.914$. The trailing-edge vortex has an opposite rotation direction to
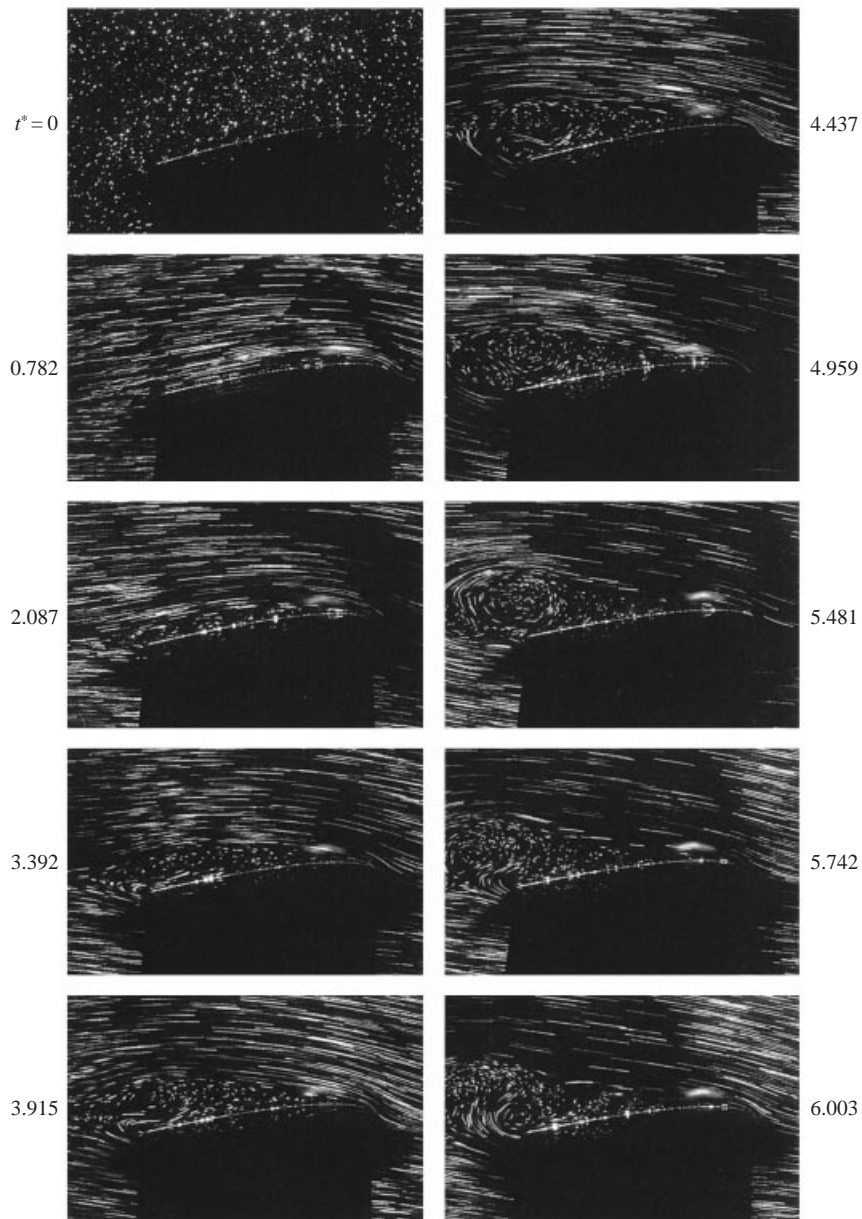
FIGURE 5. Streak pictures at $Re_c = 1200$, $\alpha = 7°$, trailing-edge vortex mode, exposure time: 0.5 s.

the escaping surface vortex. The trailing-edge vortex enlarges, and at the same time a new surface vortex is created around the mid-chord, as shown at $t^* = 4.436$ and 4.958, The new surface vortex grows and gradually rolls downstream as the trailing-edge vortex escapes from the suction surface to the wake, as shown at $t^* = 5.219$ and 6.524. The alternating shedding of the surface vortex and trailing-edge vortex continues and periodical vortex shedding in the wake is established. The sequence of characteristic flow-structure motion before the periodical vortex shedding is established includes starting vortex, boundary-layer separation, surface vortex and trailing-edge vortex.
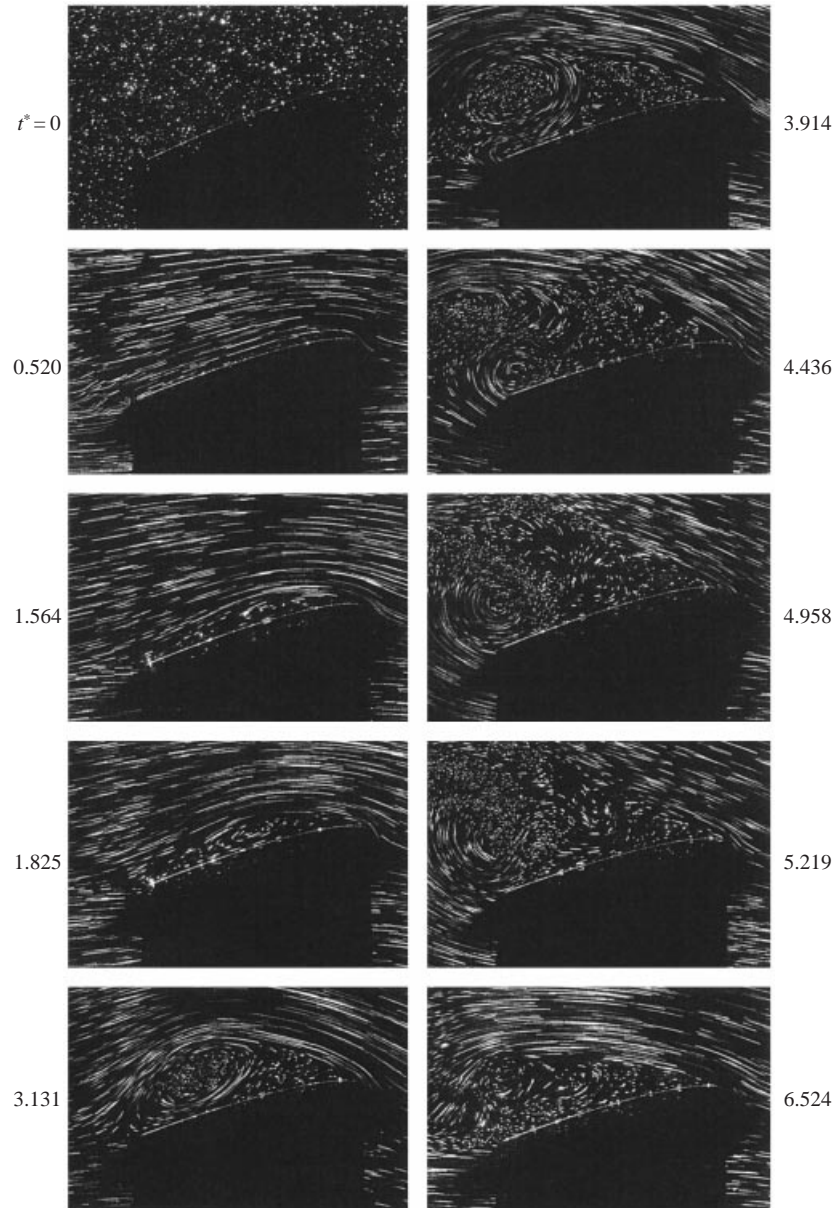
Figure 6. Streak pictures at $Re_c = 1200$, $\alpha = 15°$, separation vortex, exposure time: 0.5 s.

The *leading-edge vortex* is found in regime D of figure 3. Figure 7 shows typical streaklines of the surface flow on the suction surface. At the early stage after the start of wing motion, the starting vortex generated from the trailing edge is shed to the wake. Simultaneously, a starting vortex is generated from the leading edge. This leading-edge starting vortex does not propagate immediately to the wake region. Instead, it rolls downstream along the suction surface and evolves to become a large surface vortex, as shown at $t^* = 0.260$ and 1.043. In the meantime, two counter-rotating secondary vortices are formed upstream of the surface vortex, as shown at $t^* = 1.826$ and 2.348. At $t^* = 2.609$, the surface vortex rolls to the
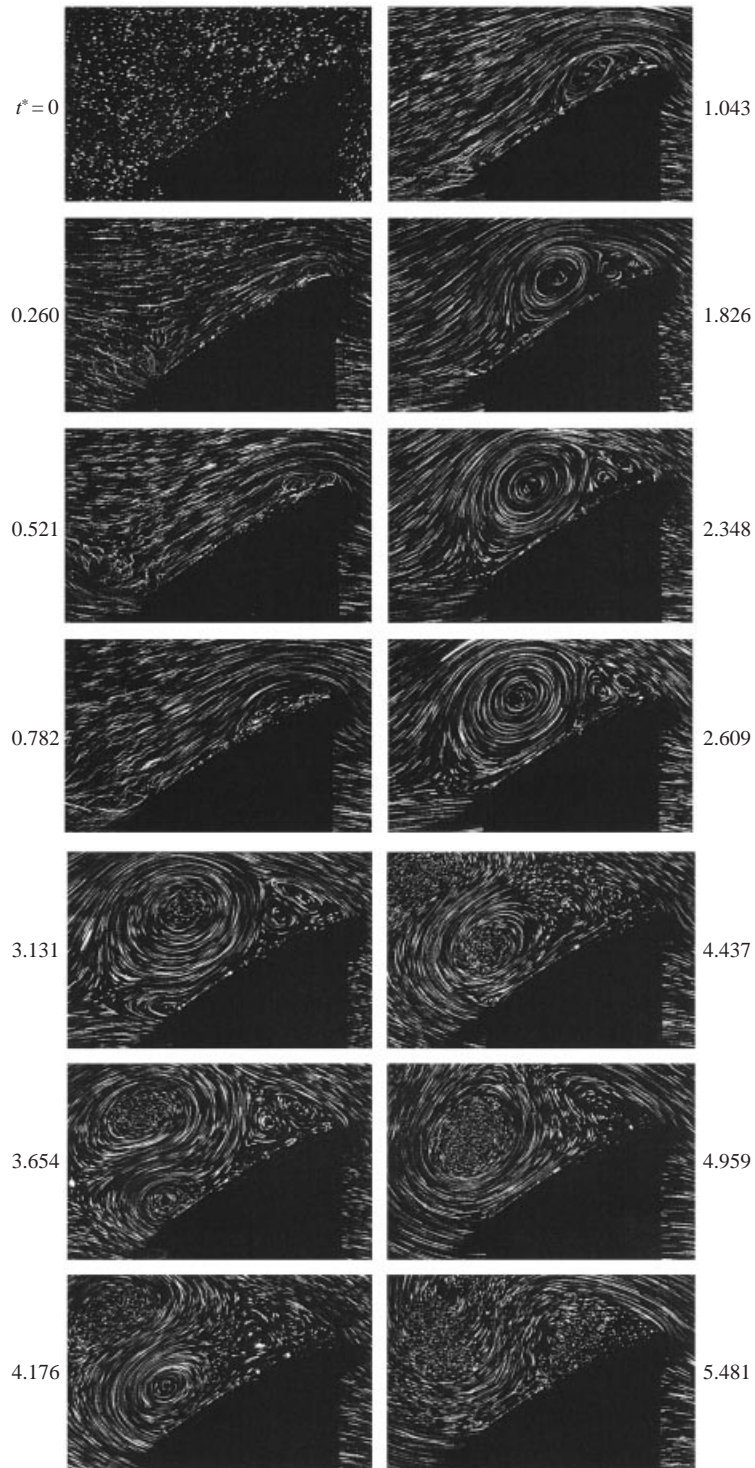
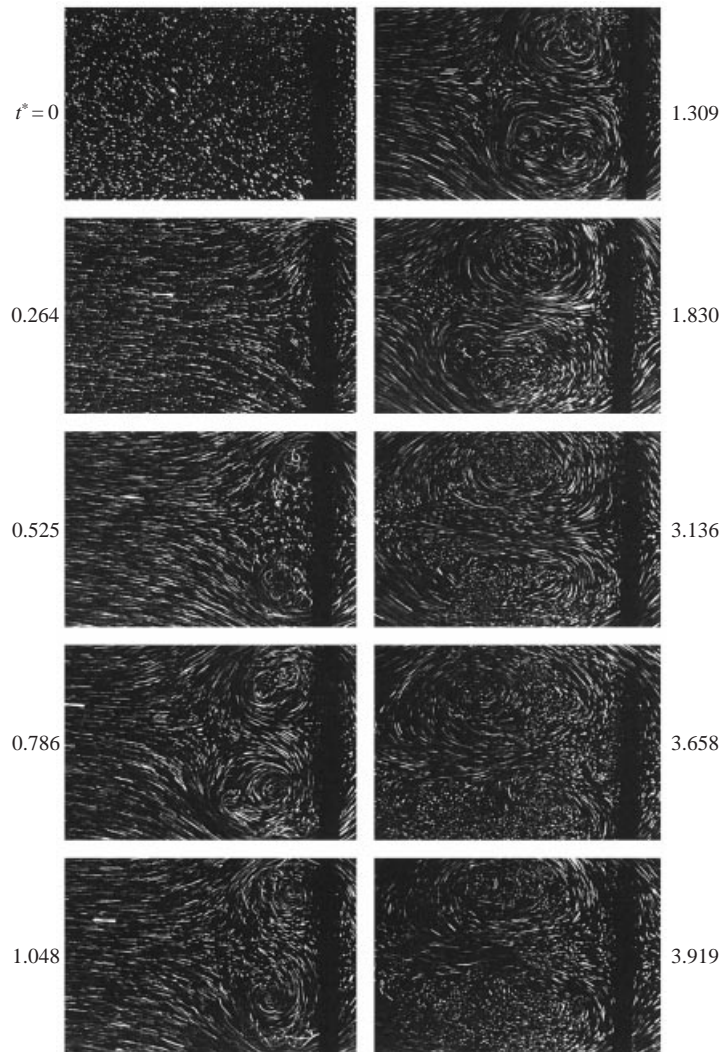FIGURE 7. Streak pictures at $Re_c = 1200$, $\alpha = 30°$, leading-edge vortex, exposure time: 0.5 s.

FIGURE 8. Streak pictures at $Re_c = 1200$, $\alpha = 90°$, bluff-body effect, exposure time: 0.25 s.

trailing edge and induces a trailing-edge vortex, which vortex grows in size as the surface vortex escapes from the wing surface, as shown at $t^* = 3.131$ to 4.176. At $t^* = 4.437$ to 5.481, the clockwise-rotating trailing-edge vortex grows, and merges with one of the secondary vortices near the leading edge, then escapes. Alternative shedding of a surface vortex and a trailing-edge vortex to the wake is therefore established.

At very large angles of attack in regime E of figure 3, the *bluff-body effect* becomes dominant. Figure 8 shows the typical streaklines of the surface flow on the suction surface. After start, the starting vortices generated from both the leading and trailing edges do not escape to the downstream area. Instead, they are attracted to the back of the wing model because of the strong bluff-body-induced low pressure in the wake, as shown at $t^* = 0.264$ and 0.525. The vortices grow unevenly and very slowly as shown at $t^* = 0.782$ to 1.830. The vortex evolving from the sharp trailing edge appears to be a little larger than the one from the leading edge due to the 'flat-face effect'
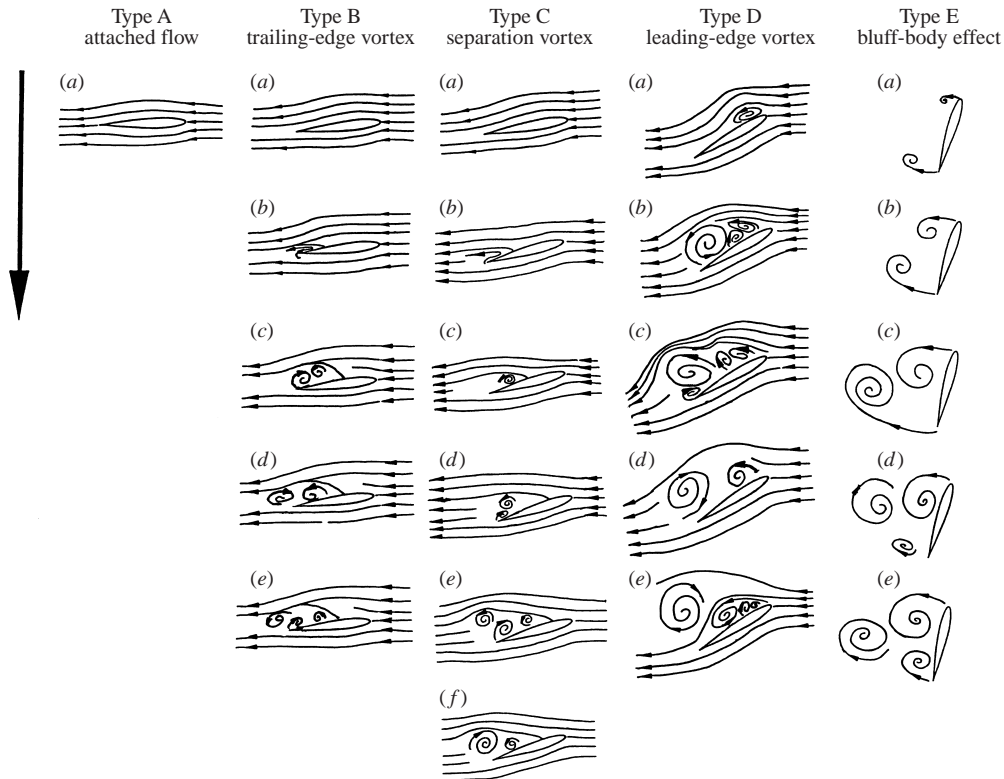
FIGURE 9. Sketches showing the evolution of various characteristic modes.

around the trailing edge (Polidori *et al.* 1992). The trailing-edge vortex grows and escapes. The growth and escape of the leading-edge vortex then follows, and the same cycle happens repeatedly. The frequency of the vortex shedding cycles in this regime appears very low compared with those in the separation vortex and leading-edge vortex regimes, due to the slow vortex formation process induced by the bluff-body effect. The process of vortex shedding in the bluff-body wake is characteristically different from those for other modes at lower angles of attack, which is more similar to the process mentioned by Polidori *et al.* on the wakes behind a semi-cylinder and a vertical flat plate.

The sketches in figure 9 show the above-mentioned primary characteristics of the evolution of flow structures on the suction surface of a NACA 0012 wing model in different regimes of Reynolds number and angle of attack. It is not intended to show topological classifications of critical points in streamline patterns, but is simply a drawing delineating the sequential motions of vortices. The topological analysis will be shown in § 3.4.

3.3. *Streamline patterns and propagation of vorticity*

All the instantaneous streamline patterns and complex evolution of the surface flows are quantitatively measured by PIV. The number of particles seeded in the water tank has been optimized to obtain good quality of measurements. Figure 10 shows a typical instantaneous velocity vector field measured by PIV in regime D at $Re_c = 1200$ and $\alpha = 30°$. Although the velocity vectors are not dense, the vortical motions of large
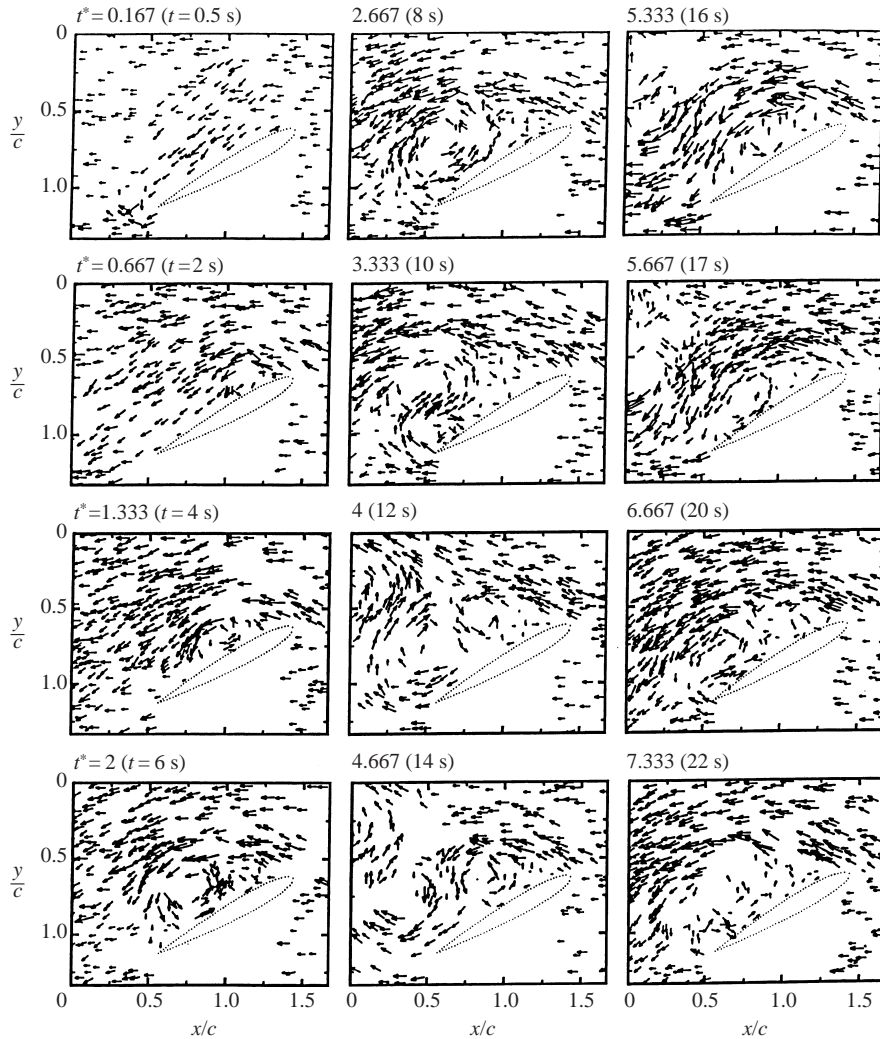
FIGURE 10. Original PIV data showing temporal and spatial evolution of velocity vectors at $Re_c = 1200$ and $\alpha = 30°$.

structures are still visible. The original randomly located velocity vectors obtained by PIV measurements are interpolated with a weighting function of $1/r^2$ to convert to a matrix form, as shown in figure 11. The visibility of dynamic vortical motions is enhanced.

In figure 12 the instantaneous streamlines are superimposed on the vector plot by the shooting method to better delineate the detailed evolution of the vortex structures. The sequence of vortex motion matches excellently the streak pictures of flow visualization shown in figure 7.

The leading- and trailing-edge starting vortices are captured at $t^* = 0.167$. At $t^* = 0.667$, the trailing-edge starting vortex rapidly escapes to the wake and goes out of view of the camera. The starting vortex from the leading edge does not propagate immediately downstream to the far wake. Instead, it rolls downstream along the suction surface and grows by entraining circumferential fluid. At $t^* = 1.333$
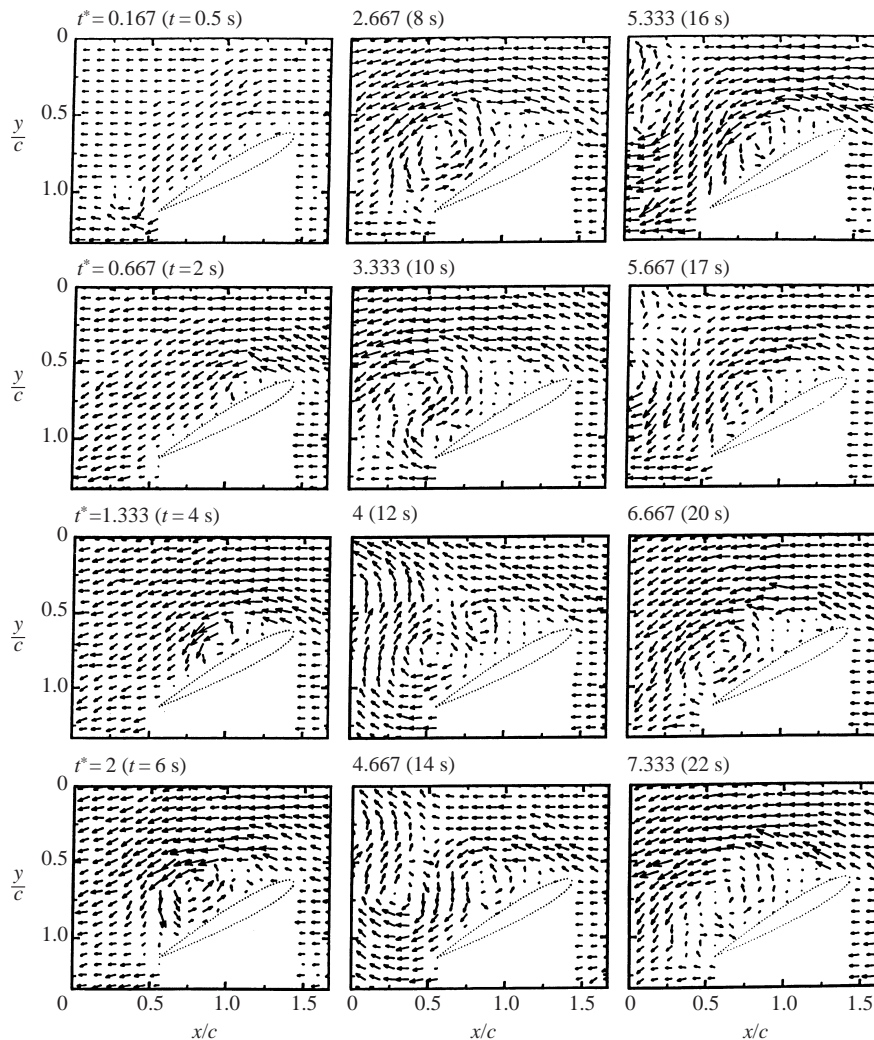
FIGURE 11. Interpolated PIV data showing temporal and spatial evolution of velocity vectors at $Re_c = 1200$ and $\alpha = 30°$.

and 2.000, two small secondary counter-rotating vortices are formed around the leading-edge area to satisfy the topological constraints. At $t^* = 2.667$, a trailing-edge vortex wrapping from the pressure surface is induced by the vortex about to escape from the suction surface. At $t^* = 3.333$ and 4.000, the surface vortex escapes, and the trailing-edge vortex enlarges. At $t^* = 4.667$ to 6.667, the trailing-edge vortex continues to enlarge and escapes from view, and a new surface vortex moves to the trailing edge and is about to escape. At $t^* = 7.333$, a new trailing-edge vortex is observed. The periodic cycle consists of the release of a surface vortex developed from the secondary vortex around the leading edge and a trailing-edge vortex induced from the pressure surface. The streamline patterns of the flow in the bluff-body effect regime in figure 13 also show detailed information of the vortex evolution process corresponding to figure 8.

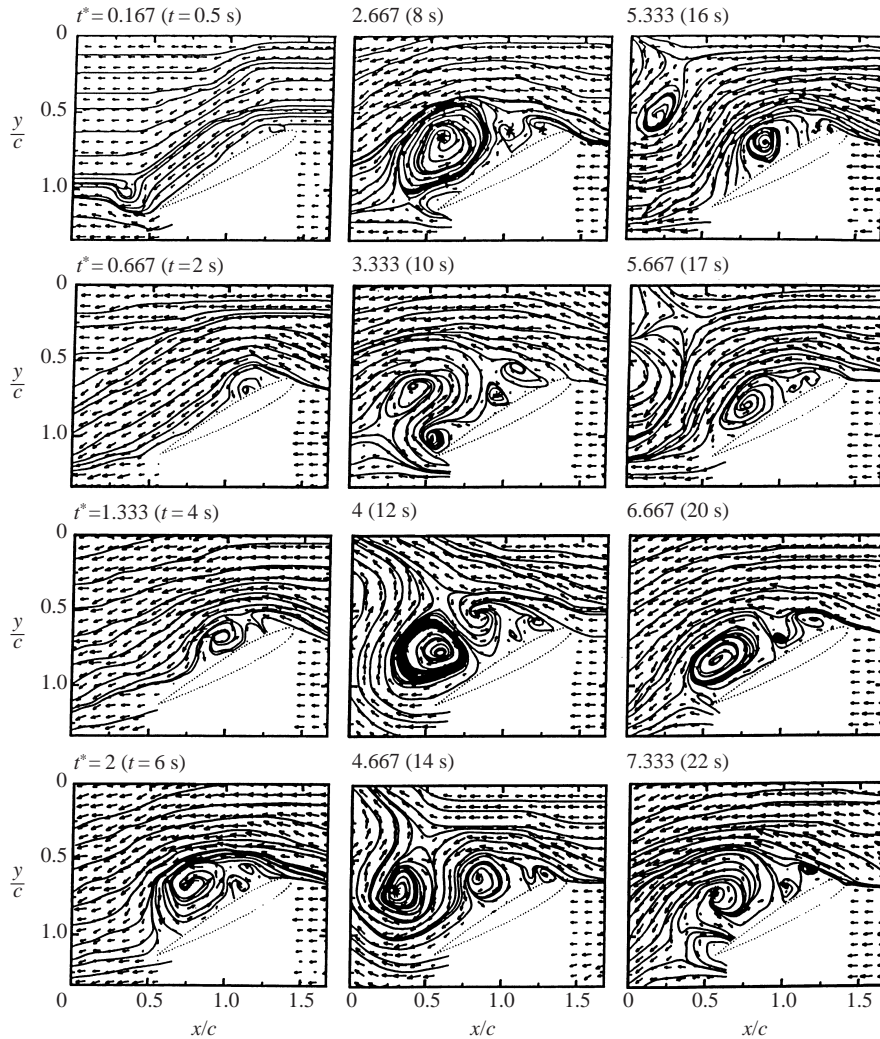The vorticity Ω_z can be calculated from the interpolated velocity data by using a

FIGURE 12. Temporal and spatial evolution of streamlines at $Re_c = 1200$ and $\alpha = 30°$ obtained from interpolated PIV data.

central difference scheme, which is defined by

$$\Omega_z = \frac{\partial v}{\partial x} - \frac{\partial u}{\partial y}, \tag{4}$$

where u and v are velocity components measured by PIV in the x- and y-directions, respectively. A vortex rotating clockwise has positive vorticity and vice versa. The propagation of vorticity corresponding to figure 12 is shown in figure 14. The four-digit numbers marked on the figure denote vorticity in units of s^{-1}. The positive vorticity 5820 around the trailing edge and the negative one -3513 around the leading edge at $t^* = 0.167$ show the starting vortices. The starting vortex generated by the trailing edge has a larger vorticity than the one generated from the leading edge owing to the sharpness of the trailing edge. The leading-edge vorticity is increased on rolling downstream to -6415 at $t^* = 0.667$ and -8540 at $t^* = 1.333$. Two weak counter-
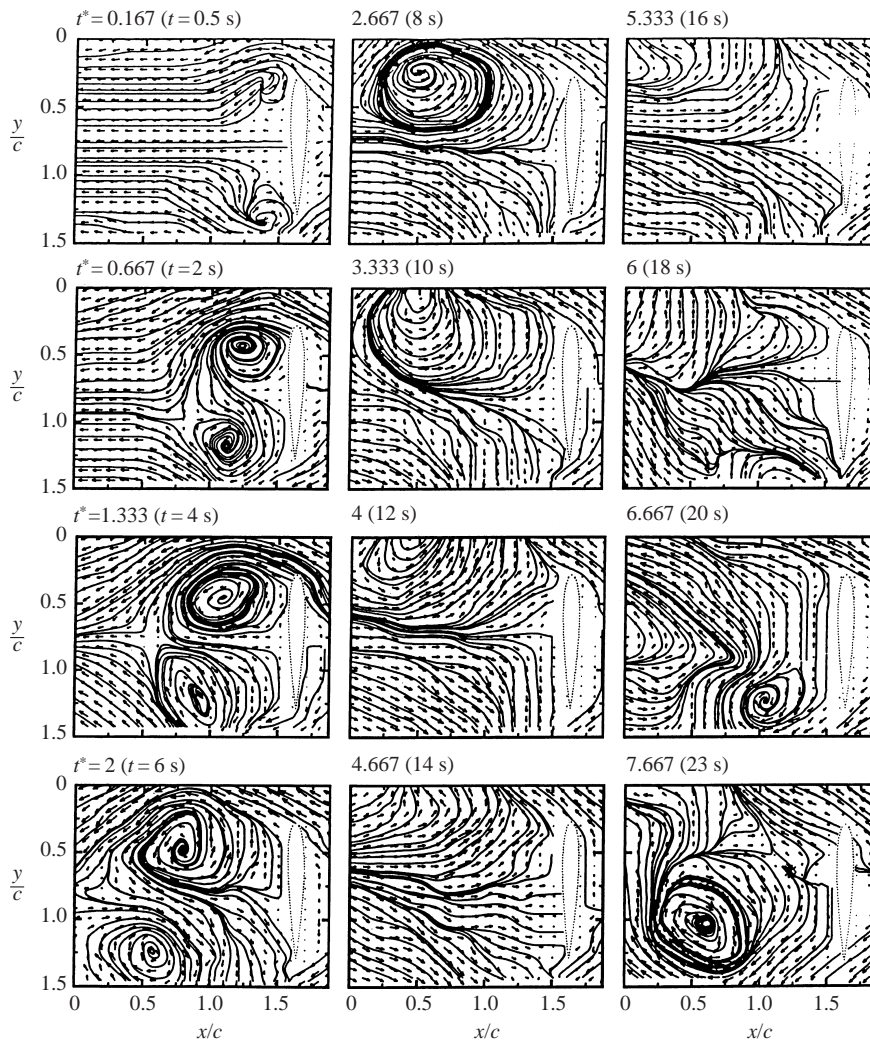
FIGURE 13. Temporal and spatial evolution of streamlines at $Re_c = 1200$ and $\alpha = 90°$ obtained from interpolated PIV data.

rotating vorticities 1457 and -5430 appear around the leading edge at $t^* = 1.333$. As time evolves, the secondary vorticity -5430 develops to a new vortex with a vorticity -6887 at $t^* = 4$. The vorticity increases when the secondary vortex develops to become a surface vortex.

3.4. *Topological analysis*

Lighthill (1963) has developed a *critical point theory* to study the no-slip flow in the vicinity of a three-dimensional separation point. A critical point is a point in a flow field where the streamline slope is indeterminate. By expressing the velocity field as a series expansion in space about the critical points, a local solution of the continuity and Navier–Stokes equations can be obtained. This solution may consist of a set of relationships between various coefficients in the expansion. Based on the local solutions, a classification of all possible regular critical points in a three-dimensional flow field can be derived. Perry and co-workers (Perry & Fairlie 1974; Chong & Perry
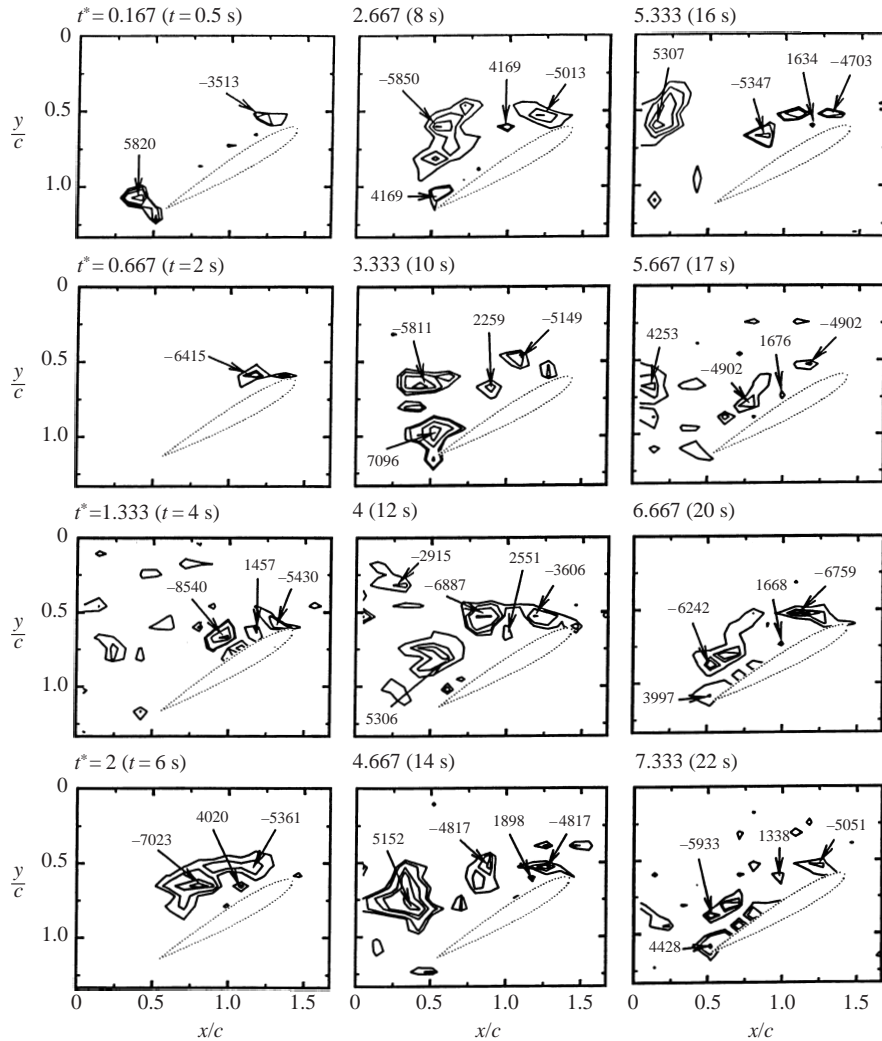
FIGURE 14. Temporal and spatial evolution of vorticity at $Re_c = 1200$ and $\alpha = 30°$. Numbers in plots denote values of vorticity in units of s^{-1}.

1990) extended the classical critical point theory to flows away from boundaries by truncating the series expansion to include only terms that were first order in the spatial coordinates. The critical points are highly relevant to eddying motions in free-shear-layer flows such as jets and wakes. By integrating the components of the three-dimensional velocity field that are resolved onto any plane that contains the critical point, 'sectional streamline patterns', including nodes, saddles, foci, bifurcation lines, and their combinations, can be obtained (Perry & Steiner 1987). The shedding process of vortices behind bluff bodies, e.g. circular cylinders and flat plates, has been topologically analysed with critical point theory by Perry *et al.* (1982), Perry & Steiner (1987) and Steiner & Perry (1987). A simple topological identification based on the present flow visualization pictures and measured streamline patterns is discussed below.

The proposed topological model of the sequence of instantaneous streamlines of
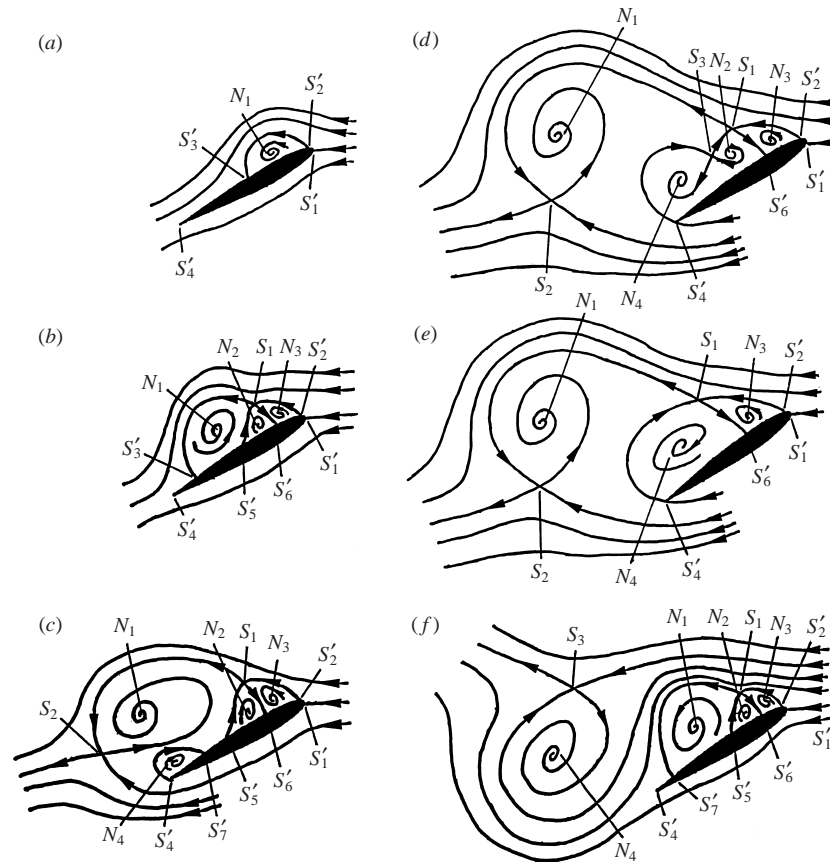
FIGURE 15. Proposed model for topological characteristics of a NACA 0012 wing starting from rest in the leading-edge-separation regime (type D). Time increases from (*a*) to (*f*).

the leading-edge vortex mode (type D) is shown in figure 15, and is characterized by separatrices, critical points and alleyways. In critical-point terminology, a *separatrix* is a streamline leaving or terminating at a saddle, and an *alleyway* is a passageway between two separatrices. In two-dimensional incompressible flow the only critical points allowed are *centres* and *saddles*, otherwise continuity is violated (Perry *et al.* 1982). Since the three-dimensional effect is almost unavoidable in real flows because the vortices are being compressed or stretched axially normal to the sectional plane of analysis (Perry & Steiner 1987), *foci* instead of centres are presented in the streamline patterns of figures 12 and 13. Topologically, a focus and centre both belong to nodes.

In figure 15(*a*), four three-way saddles, namely a stagnation point S_1' on the wing nose, a separation point S_2' near the wing nose, a reattaching point S_3', and a trailing-edge saddle S_4', are formed after start-up. In addition, a node N_1 is also shown. Subsequently, the node N_1 moves downstream, induces two counter-rotating foci, N_2 and N_3, in the upstream area, and creates an off-surface four-way saddle S_1 as well as two surface three-way saddles S_5' and S_6', as shown in figure 15(*b*). In figure 15(*c*), as the node N_1 is escaping from the wing surface, a node N_4 near the trailing edge is induced so that the three-way saddle S_3' in figure 15(*b*) is replaced by an off-surface four-way saddle S_2. A three-way saddle S_7' is shown at the reattaching point of the node N_4. In figure 15(*d*), the node N_1 is shed downstream so that the trailing-edge focus N_4 fills

the space around the trailing edge. A four-way saddle S_3 is formed between nodes N_4 and N_2, and therefore the three-way saddles S_5' and S_7' in figure 15(*c*) disappear. An alleyway moves along the wing surface. In figure 15(*e*), the node N_4 grows further, and saddle S_3 in figure 15(*d*) merges with S_1 so that the node N_2 disappears. In figure 15(*f*), node N_4 around the trailing edge is shed. The flow characteristics on the wing surface become similar to those in figure 15(*b*). As time evolves, periodic, alternating release (or shedding) of leading- and trailing-edge vortices is established. Perry & Steiner (1987) have presented the topological characteristics in the near wake behind a 45° inclined flat plate. Alternating formation and shedding of two vortices from the upper surface of the leading and trailing edges of the plate is not as complicated as that described in figure 15. The nose geometry of the wing induces small counter-rotating vortices near the leading edge, and thus complicates the whole topological plane.

Hunt *et al.* (1978) have obtained a general formula for the relationship between the number of nodes (including four-way nodes N and three-way nodes N') and saddles (including four-way saddles S and three-way saddles S') for flows around surface obstacles:

$$\left(\sum N + \frac{1}{2}\sum N'\right) - \left(\sum S + \frac{1}{2}\sum S'\right) = 1 - n, \tag{5}$$

where n is the connectivity of the section of the flow considered, which is a case-dependent parameter. In the case of a two-dimensional plane cutting a three-dimensional body, the formula becomes (Coutanceau & Pineau 1997)

$$\left(\sum N + \frac{1}{2}\sum N'\right) - \left(\sum S + \frac{1}{2}\sum S'\right) = -1. \tag{6}$$

By counting the number of three-way and four-way saddles and nodes on each plot of figure 15, for instance, $\sum N = 4$, $\sum N' = 0$, $\sum S = 2$, and $\sum S' = 6$ in figure 15(*c*), the result of equation (6) is obtained. Although the topological critical points are not shown here, the numbers of saddles and nodes in the cases of vortex evolution regimes A, B and C also satisfy equation (6).

The proposed topological model of the sequence of instantaneous streamlines of the bluff-body effect mode (type E) is shown in figure 16. The evolution of the critical points, separatrices and alleyways is similar to those in the wake of a vortical flat plate obtained by Perry & Steiner (1987). In figure 16(*a*), the starting vortices from the leading and trailing edges form two foci and three saddles on the surface. The vorticity induced by the sharp trailing edge is larger than that induced by the rounded nose of the leading edge. The geometrical imbalance makes the focus near the trailing edge larger than the one near the leading edge so that it moves downstream first, as shown in figures 16(*b*) and 16(*c*). Later, it is clearly shown in figure 16(*d*) that an eddy detached from the body near the trailing edge is forming. It becomes attached at some later stage of evolution, as shown in figure 16(*e*). Perry & Steiner have also described the role of the detached vortex during the vortex shedding process behind a vertical flat plate. Counting the numbers of saddles and nodes leads to equation (6), i.e. $\left(\sum N + \frac{1}{2}\sum N'\right) - \left(\sum S + \frac{1}{2}\sum S'\right) = -1$, which is the same as the result in the cases of surface vortex evolution regimes A, B, C and D.

The topological characteristics of flows behind a circular cylinder (Perry *et al.* 1982), vortical flat plate (Perry & Steiner 1987) and 45° inclined flat plate (Perry & Steiner 1987) are examined in figure 17. In Coutanceau & Pineau (1997), numerous results obtained from a topological analysis of particle-streak visualization on the flows over
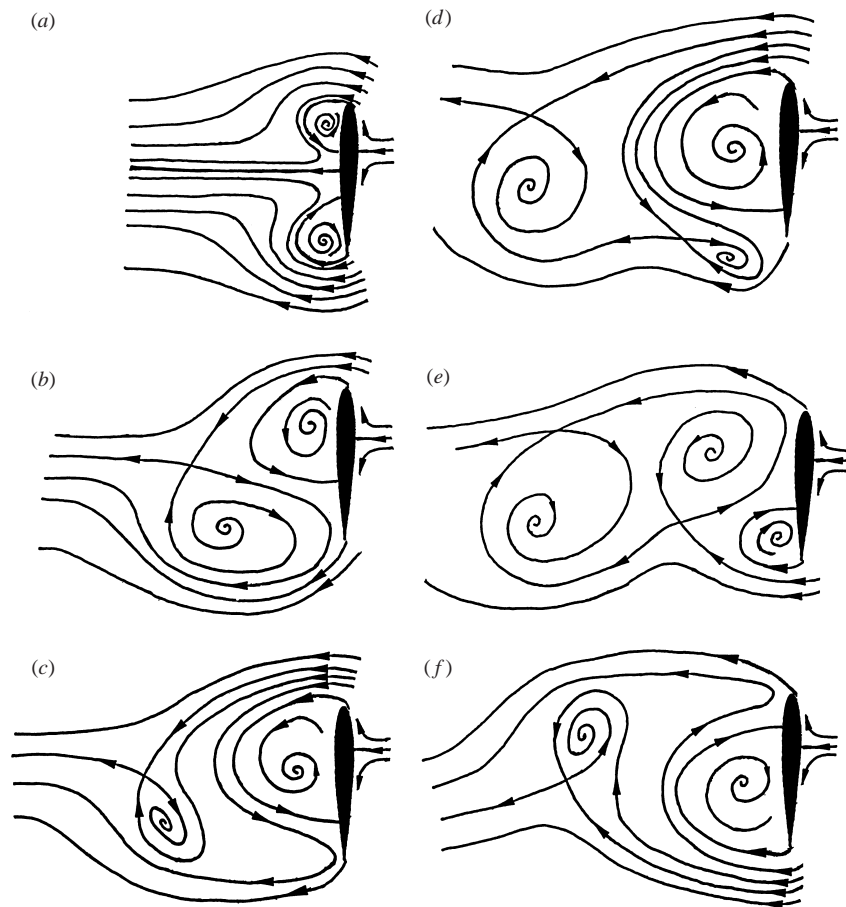
(a)

(d)

(b)

(e)

(c)

(f)

FIGURE 16. Proposed model for topological characteristics of a NACA 0012 wing starting from rest in the bluff-body-effect regime (type E). Time increases from (a) to (f).

circular cylinders and flat plates are reviewed. Details of general typical behaviour like the coalescence/splitting process, transposition of saddle points, as well as the birth, development and detachment of wake vortices for different impulsively started bluff bodies are similar to the present results for the bluff-body effect mode (type E). For other characteristic modes, the evolution processes are quite different from the bluff-body wake. These modes are strongly dependent on the angle of attack and Reynolds number.

3.5. *Characteristic time scales*

Information on the characteristic time scales and paths of vortex centres can be obtained from the PIV measured data. Figure 18(a) shows the reduced time t_s^* at the inception of separation near the trailing edge in the trailing-edge vortex and separation vortex regimes at various Reynolds numbers. It is apparent that t_s^* decreases drastically with the increase of angle of attack in the trailing-edge vortex regime. The rate of decrease is less significant in the separation vortex regime. In the trailing-edge vortex, regime t_s^* decreases with the increase of Reynolds number. However, t_s^* apparently does not change with the increase of Reynolds number in the separation vortex regime. It is clear that at small angles of attack before stall,
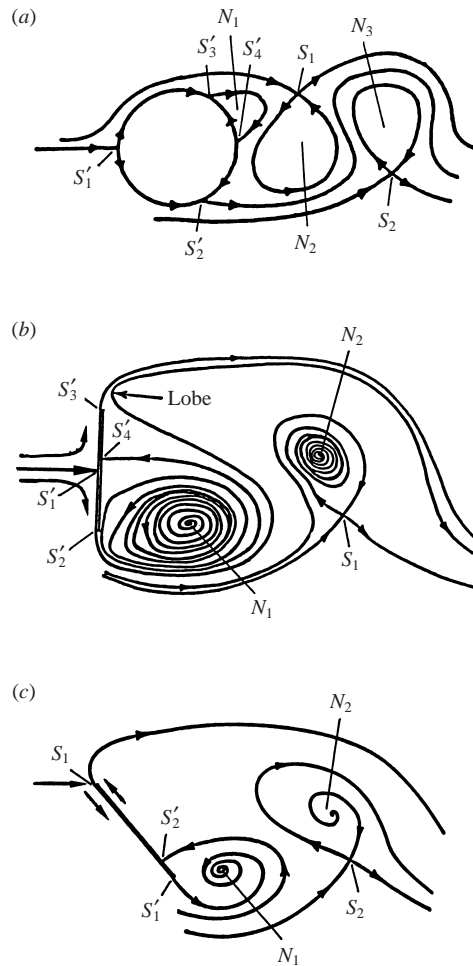
FIGURE 17. Topological characteristics of different cases: (*a*) circular cylinder (from Perry *et al.* 1982, figure 2); (*b*) vertical flat plate (from Perry & Steiner 1987, figure 9); (*c*) 45° inclined flat plate (from Perry & Steiner 1987, figure 18). Symbols *N*, *S*, and *S′*, denoting nodes and saddles have been marked by the present authors.

the inception of separation is sensitive to the angle of attack and Reynolds number. After the occurrence of stall, the inception of separation decreases broadly with the angle of attack and Reynolds number.

The reduced time t^*_{shed} for the appearance of the first trailing-edge vortex after evolution of the surface vortex, i.e. the time taken to establish stable vortex shedding, is shown in figure 18(*b*). In the separation vortex and leading-edge vortex regimes, the time taken to establish a stable vortex-shedding process decreases with the increase of angle of attack. However, the situation is reversed in the regime where the bluff-body-effect dominates. The significance of the bluff-body-effect on the characteristics of surface flow and vortex shedding depends on Reynolds number. For instance, the bluff-body effect becomes important when $\alpha > 75°$ at Reynolds number 1200, whilst at Reynolds numbers 1800 and 2400, it is already significant when $\alpha > 60°$. The reduced time t^*_{shed} may serve as an indicator of the bluff-body-effect when an object in a stream varies from slender to bluff.
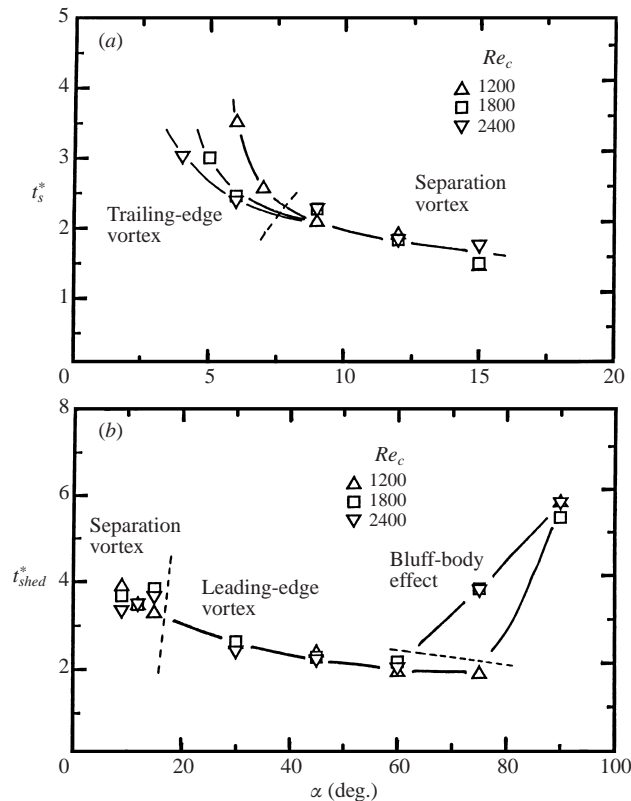
FIGURE 18. Characteristic time scales: (*a*) reduced time t_s^* at inception of separation from trailing edge after start of wing model; (*b*) reduced time t_{shed}^* at appearance of first trailing-edge vortex after evolution period of surface vortex, i.e. time taken to establish stable vortex shedding after impulsive start of wing model.

3.6. *Correlation of shedding frequency*

At low angles of attack in the attached flow regime the wing creates very small disturbances in the flow and may cause instabilities in the wake (Huang *et al.* 1996; Tritton 1988). These perturbations are usually small in the near wake and may amplify into rolled-up vortical structures in the far wake. This kind of instability is conventionally called the wake instability waves (Tritton 1988). The alternating release of a surface vortex and a trailing-edge vortex from the suction surface of the wing model in the separation vortex, leading-edge vortex and bluff-body effect regimes causes periodic instabilities in the wake, which are conventionally called vortex shedding (Tritton 1988). In the literature the term 'vortex shedding' has sometimes been employed for all wake instabilities irrespective of how the vortical structures in the wake have evolved. The shedding frequency f varies with the angle of attack α and Reynolds number Re_c, as shown in figure 19. Large angle of attack has a negative effect on the frequency of vortex shedding. However, large Reynolds number increases shedding frequency.

When discussing the dynamic behaviour of the flow in the wake, the width of the wake is a physically meaningful length scale to obtain a universal law. However, since the wake width is a function of the physical width d, which is the length of the wing-section projection on the cross-stream plane, and because it is difficult to
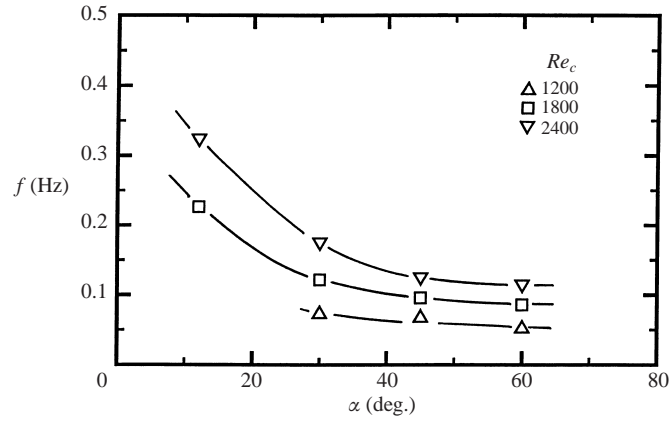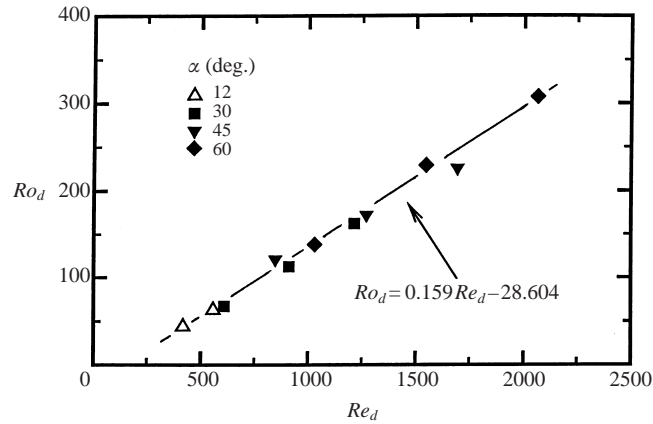
FIGURE 19. Frequency of alternating vortex release.

FIGURE 20. Functional relationship between Roshko number Ro_d and Reynolds number Re_d.

define and apply, the physical width d is commonly used. The frequency f in figure 19 can be correlated by the Roshko number $Ro_d \equiv fd^2/v$ and the Reynolds number $Re_d \equiv u_w d/v$, based on the length scale d and kinetic viscosity of water v. The Roshko number has been adopted by many investigators to correlate periodic wakes (Roshko 1955; Berger & Wille 1972; Simmons 1977; Levi 1983). In the viscous-dominated regime, e.g. at very low Reynolds numbers, the Roshko number of the instability waves should remain constant. Huang & Lee (2000) have experimentally obtained a constant Roshko number for a wing at very low Reynolds numbers and angles of attack.

In figure 20, the Roshko number Ro_d increases linearly with the increase of Reynolds number Re_d. Apparently, the vortex shedding in the wake at the present Reynolds numbers is beyond the regime of an instability wave which is dominated by viscosity, so that a constant value of Roshko number is not obtained. The regression equation is

$$Ro_d = 0.159 Re_d - 28.604. \tag{7}$$

Another frequently used non-dimensional group to correlate dynamic data in the wake is the Strouhal number St_d, which is defined by $St_d \equiv fd/u_w$. It can remain
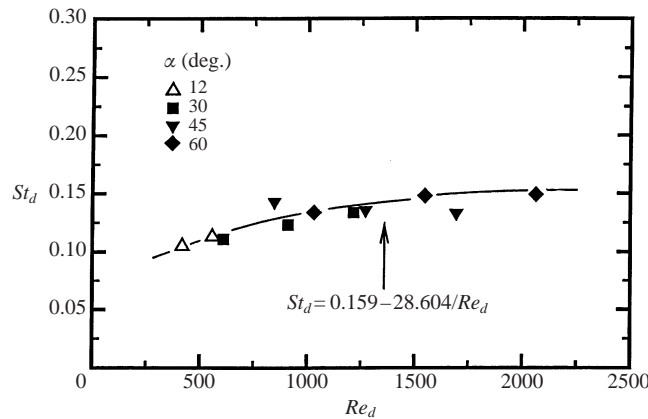
FIGURE 21. Functional relationship between Strouhal number St_d and Reynolds number Re_d.

a constant in the inertial-dominated regime. For instance, a constant value of about 0.212 is traditionally taken for a circular cylinder in cross-flow at sufficiently large Reynolds numbers less than 3×10^5 (Linhard 1966). The definitions of the Strouhal, Roshko and Reynolds numbers gives the following relationship:

$$St_d = Ro_d/Re_d. \tag{8}$$

Hence, on dividing by Re_d, equation (7) becomes

$$St_d = 0.159 - 28.604/Re_d. \tag{9}$$

The results are shown in the fitted curve of figure 21. The Strouhal number increases with the Reynolds number when $Re_d < 1500$, then becomes almost constant when the Reynolds number is large. The maximum Strouhal number would be about a constant 0.159 in the inertial-dominated regime as predicted by equation (9). Thus, the current experiment is not within either of the limiting regimes where viscosity or inertia totally dominates.

Roshko (1954) has experimentally obtained two well-known equations for the non-dimensional frequency St_d of Kármán vortex shedding in the wake of a circular cylinder:

$$St_d = 0.212 - 4.5/Re_d \quad (50 < Re_d < 150), \tag{10}$$

$$St_d = 0.212 - 2.7/Re_d \quad (300 < Re_d < 2000). \tag{11}$$

The Strouhal number of the cylinder wake would approach 0.212 as the Reynolds number approaches infinity. Novak (1973) has measured the instabilities in a two-dimensional wake behind a sharp-edged flat plate. The maximum Strouhal number is 0.150 at Reynolds number 10 000. Roshko (1955) and Simmons (1977) introduced a 'universal' Strouhal number St^* based on the measured wake width d^* for several types of two-dimensional bluff bodies. They found $St^* = 0.163$. Levi (1983) justified Roshko and Simon's universal Strouhal law by modelling the available specific kinetic energy $u^2/2$ of the oscillating fluid with the specific mechanical energy $(2\pi f d^*)^2/2$ of an oscillator which oscillates at frequency f within the width d^*. The universal Strouhal number St^* thus became $(1/2)\pi = 0.159$. The result of the energy model seems to be very close to that of the current experiments.

On comparing these results, it appears that the curvature at the ends of an object raises the Strouhal number of vortex shedding in the wake. The wing employed in

the present study has a round leading edge (although the curvature diameter is very small) and a sharp trailing edge, and the value of maximum Strouhal number is between those of a circular cylinder and a flat plate. The reason may be found in the shear-layer instability waves in the separated boundary layers from the curvatured surfaces (Roshko 1955; Simmons 1977).

4. Summary and conclusions

(1) The evolution of surface flows on the suction surface of an impulsively started NACA 0012 wing in the parameter domain of towing velocity/angle of attack presents complex multi-modes: attached, trailing-edge vortex, separation vortex, leading-edge vortex and bluff-body effect.

(2) In the trailing-edge vortex regime, the vortex shedding starts from the release of a trailing-edge vortex and is followed by a surface vortex induced in the separated boundary layer. In the separation vortex regime, the vorticity in the separated boundary layer is large enough to form a structured surface vortex before the trailing-edge vortex is induced. The surface vortex rolls downstream along the wing chord and induces a trailing-edge vortex on shedding. In the leading-edge vortex regime, the surface vortex is formed from the starting vortex of the leading edge. The alternating shedding of surface and trailing-edge vortices is similar to that in the separation vortex regime. At very large angles of attack, the starting vortices evolving from both the leading and trailing edges are attracted by the large sub-atmospheric pressure behind the wing model and become two large surface vortices, which evolve slowly and eventually escape alternatingly to form periodic shedding.

(3) The alternating shedding of the surface vortex and trailing-edge vortex in the trailing-edge vortex, separation vortex and leading-edge vortex regimes as well as the large surface vortices in the bluff-body effect regime cause periodic instabilities in the wake. At large Reynolds numbers in the inertial-dominated regime, the Strouhal number of vortex shedding of the NACA 0012 wing would attain a constant 0.159, which is a little larger than the maximum Strouhal number 0.15 for a vertical flat plate and is lower than the 0.212 of a circular cylinder. The sharper the end of the object, the smaller the maximum Strouhal number obtained.

(4) In the streamlines on a two-dimensional plane cutting a three-dimensional body, the singular points follow the topological rule

$$\left(\sum N + \frac{1}{2} \sum N'\right) - \left(\sum S + \frac{1}{2} \sum S'\right) = -1,$$

as obtained by Hunt *et al.*

REFERENCES

ABBOT, I. H. & VON DOENHOFF, A. E. 1959 *Theory of Wing Section*, pp. 113–115. Dover.

ARENA, A. V. & MUELLER, T. J. 1980 Laminar separation, transition, and turbulent reattachment near the leading edge of airfoils. *AIAA J.* **18**, 747–753.

BERGER, E. & WILLE, R. 1972 Periodic flow phenomena. *Ann. Rev. Fluid Mech.* **4**, 313–340.

BROOKS, T. F. & SCHLINKER, R. H. 1983 Progress in rotor broadband noise research. *Vertica* **7**, 287–307.

CHEN, R. C. & FAN, L.-S. 1992 Particle image velocimetry for characterizing the flow structure in three dimensional gas-liquid-solid fluidized beds. *Chem. Engng Sci.* **47**, 3615–3622.

CHONG, M. S. & PERRY, A. E. 1990 A general classification of three-dimensional flow fields. *Phys. Fluids* A **2**, 765–777.

CHU, C.-C., CHANG, C.-C., LIU, C. C. & CHANG, R. L. 1996 Suction effect on an impulsively started circular cylinder: vortex structure and drag reduction. *Phys. Fluids* A **8**, 2995–3007.

CHU, C.-C. & LIAO, Y.-Y. 1992 A quantitative study of the flow around an impulsively started circular cylinder. *Exps Fluids*, **13**, 137–146.

COUTANCEAU, M. & MENARD, C. 1985 Influence of rotation on the near-wake development behind an impulsively started circular cylinder. *J. Fluid Mech.* **158**, 299–446.

COUTANCEAU, M. & PINEAU, G. 1997 Some typical mechanisms in the early phase of the vortex-shedding process from particle-streak visualization. In *Atlas of Visualization III* (ed. Y. Nakayama & Y. Tanida), pp. 43–68. CRC Press.

DAVIS, J. C. 1986 *Statistics and Data Analysis in Geology*. John Wiley & Sons.

GERICH, D. & ECKELMANN, H. 1982 Influence of end plates and free ends on the shedding frequency of circular cylinders. *J. Fluid Mech.* **122**, 109–121.

HUANG, R. F. & LEE, H. W. 2000 Turbulence effect on frequency characteristics of unsteady motions in wake of wing. *AIAA J.* **38**, 87–94.

HUANG, R. F. & LIN, C. L. 1995 Vortex shedding and shear-layer instability of wing at low-Reynolds numbers. *AIAA J.* **33**, 1398–1430.

HUANG, R. F., SHY, W. W., LIN, S. W. & HSIAO, F. B. 1996 Influence of surface flow on aerodynamic loads of a cantilever wing. *AIAA J.* **34**, 527–532.

HUANG, J. C. R., ABELL, C. J., PETERKA, J. A. & WOO, H. 1978 Kinematical studies of the flows around free or surface-mounted obstacles; applying topology to flow visualization. *J. Fluid Mech.* **86**, 299–446.

LEVI, E. 1963 A universal Strouhal law. *ASCE J. Engng Mech.* **109**, 718–727.

LIGHTHILL, M. J. 1963 *Laminar Boundary Layers* (ed. L. Rosenhead), pp. 48–88. Oxford University Press.

LINHARD, J. H. 1966 Synopsis of lift, drag, and vortex frequency data for rigid circular cylinders. *Res. Div. Bull.* 300. Washington State University, College of Engineering.

LISSAMAN, P. B. S. 1983 Low Reynolds number airfoils. *Ann. Rev. Fluid Mech.* **15**, 223–239.

TA PHUOC LOC & BOUARD, R. 1985 Numerical solution of the early stage of the unsteady viscous flow around a circular cylinder: a comparison with experimental visualization and measurements. *J. Fluid Mech.* **160**, 93–117.

NAIR, M. T. & SENGUPTA, T. K. 1997 Unsteady flow past elliptic cylinders. *J. Fluids Struct.* **11**, 555–595.

NOVAK, J. 1973 Strouhal number and flat plate oscillation in an air stream, *Acta Technica Csav* **4**, 372–386.

OERTEL, H., JR. 1990 Wakes behind blunt bodies. *Ann. Rev. Fluid Mech.* **22**, 539–564.

OHMI, K., COUTANCEAU, M., DAUBE, O. & TA PHUOC LOC 1991 Further experiments on vortex formation around an oscillating and translating airfoil at large incidences. *J. Fluid Mech.* **225**, 607–630.

OHMI, K., COUTANCEAU, M., TA PHUOC LOC & DULIEU, A. 1990 Vortex formation around an oscillating and translating airfoil at large incidences. *J. Fluid Mech.* **211**, 37–60.

PERRY, A. E., CHONG, M. S. & LIM, T. T. 1982 The vortex-shedding process behind two-dimensional bluff bodies. *J. Fluid Mech.* **116**, 77–90.

PERRY, A. E. & FAIRLIE, B. D. 1974 Critical points in flow patterns. *Adv. Geophys.* B **18**, 299–315.

PERRY, A. E. & STEINER, T. R. 1987 Large-scale vortex structures in turbulent wakes behind bluff bodies. Part 1. Vortex formation. *J. Fluid Mech.* **174**, 233–270.

POLIDORI, G., PINEAU, G., MRAIM, K. A. & COUTANCEAU, M. 1992 Shedding process of the initial vortices from impulsively started cylinders at $Re = 1000$: end and body geometry effects. In *Bluff-Body Wakes, Dynamics and Instabilities, IUTAM Symp.*, pp. 284–288. Springer.

RICHARD, C. F. & JOHN, H. S. 1988 *Fundamentals of Air Pollution Engineering*, pp. 290–357. Prentice Hall.

ROSHKO, A. 1954 On the drag and shedding frequency of two-dimensional bluff-bodies. *NACA Tech. Note* 3169.

ROSHKO, A. 1955 On the wake and drag of bluff bodies. *J. Aero. Sci.* **22**, 124–135.

SIMMONS, J. E. L. 1977 Similarities between two-dimensional and axisymmetric vortex wakes. *Aero. Q.* **26**, 15–20.

SLAOUTI, A. & GERRARD, J. H. 1981 An experimental investigation of the end effects on the wake

of a circular cylinder towed through water at low Reynolds numbers. *J. Fluid Mech.* **112**, 297–314.

SPEDDING, G. R. & RIGNOT, E. J. 1993 Performance analysis and application of grid interpolation techniques for fluid flows. *Exps Fluids*, **15**, 417–430.

STEINER, T. R. & PERRY, A. E. 1987 Large-scale vortex structures in turbulent wakes behind bluff bodies. Part 2. Far-wake structures. *J. Fluid Mech.* **174**, 271–298.

STUBER, K. & GHARIB, M. 1988 Experiment on the forced wake of an airfoil transition from order to chaos. *AIAA Paper* 88-3840.

SUMNER, D., PROCE, S. J. & PAIDOUSSIS, M. P. 1997 Investigation of impulsively-started flow around side-by-side circular cylinders: application of particle image velocimetry. *J. Fluids Struct.* **11**, 597–615.

TRITTON, D. J. 1988 *Physical Fluid Dynamics*, pp. 243–277. Oxford University Press.

WILLIAM, C. H. 1982 *Aerosol Technology*. Academic.

WILLIAMSON, C. H. K. 1996 Vortex dynamics in the cylinder wake. *Ann. Rev. Fluid Mech.* **28**, 477–539.